

Available online at www.sciencedirect.com

Computers and Structures xxx (2006) xxx–xxx

**Computers
& Structures**
www.elsevier.com/locate/compstruc

On the initial configurations of collapsible channel flow

Xiaoyu Luo ^{*}, Ben Calderhead, Haofei Liu, Wenguang Li

Department of Mathematics, University of Glasgow, Glasgow Q12 8QW, UK

Received 1 June 2006

Abstract

This paper studies the effect of the initial configurations of the governing equations on flows in a collapsible channel where the upper elastic wall is replaced by a pre-stretched beam. The aim is to check the existence of a “tongue” shaped neutral stability curve in the Reynolds number – tension space from a fluid-beam model [Luo XY, Cai ZX. Effects of wall stiffness on the linear stability of flow in an elastic channel. In: de Langre E, Axisa F, editors. Proceedings of the 8th international conference on fluid induced vibrations, FIV2004, vol. II. Paris, France: 2004. p. 167–70], in a properly formulated initial strain configuration. It was found that, for a given Reynolds number, as the tension is lowered to a critical value, the system becomes unstable, which is to be expected. However, a further decrease of the tension re-stabilizes the system before it becomes unstable again. It was possible that this puzzling finding was an artefact since the elastic equations used in the model were not properly derived from the zero initial stress configuration (Ogden, private communication). In this paper, a range of steady solutions are studied with both zero and non-zero initial wall tension. These are compared with the results using the finite element package Adina 8.3 using both the initial strain and initial stress configurations. As expected, the fluid-beam model agrees with Adina when using the initial stress configuration, but not when using the initial strain configuration. For cases with a small initial tension or small deformation (very large initial tension), both initial stress and initial strain configurations lead to very similar results, however, when the initial tension is comparable with the stretching induced tension, there are obvious differences in these two configurations. The “tongue” stability curve is then re-calculated with a zero initial tension, and re-plotted in the re-effective tension number space. It is interesting to see that though slightly different in shape, the “tongue” stable zone appears again when the zero initial tension is used. Thus it is highly likely that the puzzling “tongue” in the neutral stability curve is not due to the modelling approximation, but indicating a real, interesting physical phenomenon.

© 2006 Published by Elsevier Ltd.

Keywords: Initial stress; Initial strain; Collapsible channel flow; Finite element methods; Neutral stability; Eigenvalue problem; Fluid–structure interactions

1. Introduction

Flow in collapsible tubes has been extensively studied in the last few decades, not only for its relevance to physiological applications, but also for the interesting fluid–structure interactions that occur in the system [2]. Self-excited oscillations in such a system are frequently observed in the laboratory in a “Starling resistor” [13,14]. Similar oscillations have also been reproduced using one-dimensional [15,16], or two-dimensional models [17–20]. Due to extensive com-

putational requirements, to date except for steady or simplified simulations [20], there have been almost no reports on self-excited oscillations in truly three-dimensional models, which would be desirable to make full quantitative comparisons with experiments. However, it is believed that simple 1-D and 2-D models, though some based on rather crude approximations, can serve to shed light on many important features of the dynamics of the system.

The fluid-membrane model employed by Luo and Pedley [17–20], like other similar two-dimensional models of this type, suffers from several *ad hoc* approximations: the membrane was inextensible, the bending wall stiffness was ignored, and the elastic wall was assumed to move either

^{*} Corresponding author. Tel.: +44 141 3304746; fax: +44 141 3304111.
E-mail address: x.y.luo@maths.gla.ac.uk (X. Luo).

51 in the vertical or in the normal direction. Although these
52 may be adequate for steady flow simulations, their influ-
53 ence on unsteady flows, especially on the self-excited
54 oscillations, needs to be carefully evaluated. Recently, a
55 fluid-beam model in which the membrane is replaced by
56 a plane strained elastic beam with large deflection has been
57 put forward by Cai and Luo [24]. In this model the two-
58 dimensional solid mechanics of the wall is taken into
59 account, thus avoiding the above *ad hoc* assumptions. An
60 ALE (Arbitrary Lagrangian Eulerian) solver combined
61 with a method of rotating spines was used to solve the
62 two-dimensional Navier–Stokes equations fully coupled
63 with the two-dimensional non-linear large displacement
64 structural equations [24]. Extending this model to study
65 unsteady motions, Luo and Cai [1] discovered that the
66 system gives rise to various different types of self-excited
67 oscillations. It is found that the small amplitude oscilla-
68 tions are in excellent agreement with those predicted by
69 solving the linearized Orr–Sommerfeld equations of the
70 system perturbed around the numerically simulated large
71 deformation steady solutions. Most interestingly, they
72 found an intriguing “tongue” shaped neutral stability
73 curve in the Reynolds number-tension space, see Fig. 1.

74 This curve shows that, for a given Re , the beam is stable
75 for a large value of the longitudinal initial tension, and
76 unstable when the tension is below a certain level. How-
77 ever, inside the unstable zone when tension is lower than
78 a critical value, there exists a tongue shaped zone when
79 the system becomes stable again. As it seems bizarre that
80 reducing the tension may re-stabilize the system, it is natu-
81 ral to ask if this is really physical or due to a flaw in the
82 model. In fact, it is possible that this puzzling finding was
83 an artifact, because the elastic equations used in the model

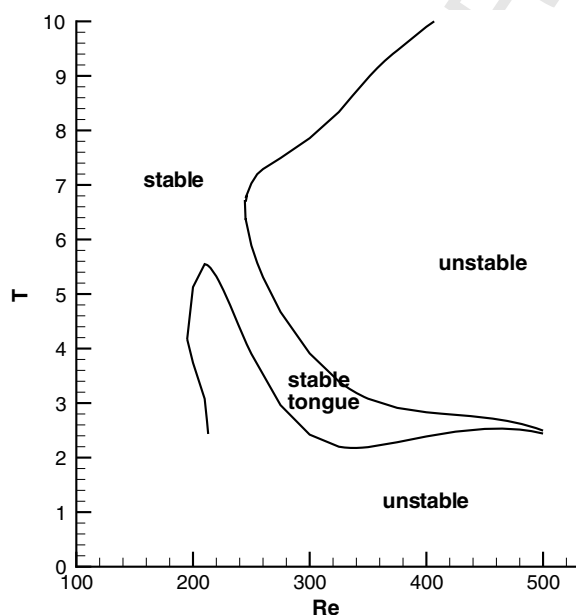


Fig. 1. The neutral stability curve in Re – T space predicted by [1] for $c_l = 600$, and $p_e = 1.95$ (see text for parameter definitions). Note there is a stability “tongue” sandwiched by the otherwise unstable regions.

were not properly derived from the zero initial stress con- 84
figuration (we are grateful to Professor R.W. Ogden for 85
pointing this out). The concept of the eigensolution of 86
the system is essentially based on the energy arguments 87
(the total energy must be minimum), which is only valid 88
for solid equations derived from a zero initial stress con- 89
figuration [25]. However in the fluid-beam model (as is com- 90
monly done by many other two-dimensional models), the 91
initial stress approach is used [1,24]. In other words, does 92
the “tongue” exist if the initial stress is free? This paper 93
aims to answer this question and investigate the effects of 94
the initial configurations on the steady solutions and on 95
the neutral curve. 96

2. The initial strain and initial stress configurations 97

The model consists of a steady flow in a channel in 98
which a part of the upper wall is replaced by an elastic 99
beam, see Fig. 2. The rigid channel has width D , a part 100
of the upper wall with length L is replaced by a pre-stressed 101
elastic beam subjected to an external pressure p_e . L_u and L_d 102
are the lengths of the upstream and downstream rigid part 103
of the channel. Steady Poiseuille’s flow with average velocity 104
 U_0 is assumed at the entrance. The flow is incompress- 105
ible and laminar, the fluid having density ρ and viscosity μ . 106
The extensional and bending stiffness of the beam are EA 107
and EJ , respectively, where E is the Young’s modulus,¹ A 108
is the thickness of the beam, and J is the bending moment. 109
The pre-tension in the beam (caused by an initial stretch of 110
the beam) is T and the density of the beam is ρ_m . Damping 111
and rotational inertia of the beam are both neglected. 112

If the initial length of the elastic wall is l_0 , see Fig. 3, and 113
the length between the two rigid walls is l , then for zero initial 114
stress, $l_0 = l$. The principal stretch is then defined as 115
 $\lambda = ds/dZ$, see Fig. 3. However, if there is an initial stretch, 116
then $l_0 < l$, and 117

$$\lambda = \frac{ds}{dZ_0} = \frac{ds}{dZ} \frac{dZ}{dZ_0} = \lambda_x \lambda_0, \quad (1) \quad 120$$

where $\lambda_x = ds/dZ$ is the stretch defined with l . It is impor- 121
tant to realize that unless $\lambda_0 = 1$ (i.e. $Z_0 = Z$), $\lambda \neq \lambda_0 \neq \lambda_x$. 122
If the principal stretch is defined with the initial length l_0 , as 123
in (1), this is known as the initial strain formulation. The 124
other typical method used in solid mechanics is so called 125
the initial stress formulation. In this formulation, the initial 126
tension does not cause any deformation, and the principal 127
stretch is defined with the deformed length l , i.e., λ_x , rather 128
than λ , is used. However to account for the effect of the ini- 129
tial deformation, an initial stress $\sigma_0 (= T/A)$ is added to the 130
stress in the governing equations. Note, the initial strain 131
formulation is defined with the initial zero stress configura- 132
tion. The stretching energy for this case can be written as 133

¹ As, we consider a plane strain problem here, E here is equivalent to the 134
conventional Young’s modulus divided by $(1 - \nu^2)$, where ν is the 135
Poisson’s ratio.

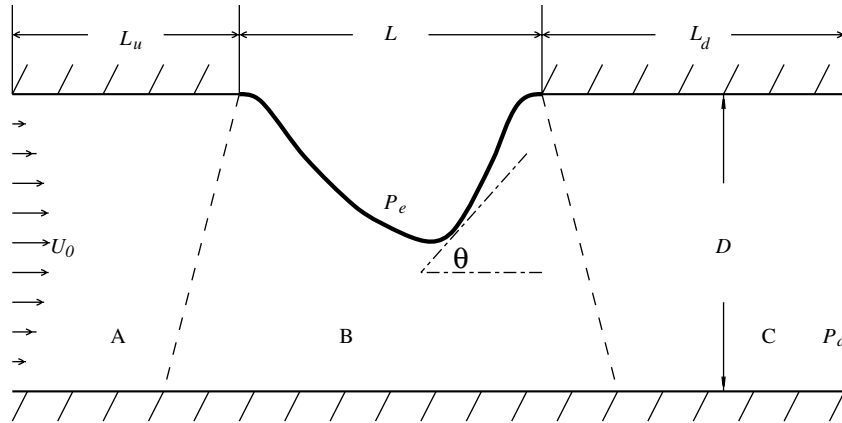


Fig. 2. The flow-beam configuration (not to scale). Part B has part of the wall being replaced by an elastic beam.

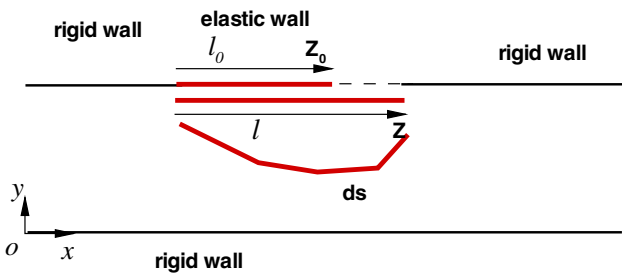


Fig. 3. Definition of the initial configurations.

$$\frac{1}{2} c_\lambda (\lambda - 1)^2 = \frac{1}{2} c_\lambda (\lambda_0 \lambda_x - 1)^2. \quad (2)$$

It is noted that the initial stress configuration is only an approximation of the original problem and its stretching energy is $\frac{1}{2} c_\lambda (\lambda_x - 1)^2$, which is not the same as (2) unless $\lambda_0 = 1$. However, this formulation is commonly used in many previous models [8]. In addition, it is often assumed that the tension is constant along the elastic wall, i.e., the additional tension induced by deformation and fluid stresses is negligible, thus $\lambda = \lambda_0 = \text{constant}$. Some models also assumed that the wall moves only in the y -direction [25]. These are all valid approximations provided the wall deformation is small. However, for large deformation, non-linear, problems, if the stability analysis is carried out on an eigenproblem which is based on energy argument, it is important that the strain energy is calculated using the principal stretch defined by Eq. (1) [25], in other words, the initial strain formulation should be employed.

The strategy of the study is as follows. First, the results from the fluid-beam model will be compared with that of the commercial finite element package Adina 8.2, for the same model problem, using both the initial stress and initial strain configurations. The differences between these results will be discussed. Then a new neutral curve for the problem with a zero initial tension will be computed, as this implies that $\lambda = \lambda_x$ ($\lambda_0 = 1$). This new neutral curve will then be compared with that of the old curve, in order to identify the existence of the ‘‘tongue’’.

3. Governing equations

3.1. The governing equations for the fluid-beam model

For convenience, the flow velocity components u_i , fluid stresses σ_i , pressure p , time t , the Cartesian coordinates x , y (originated at the left bottom of the channel), and length l are non-dimensionalized as follows:

$$\begin{aligned} u_i^* &= \frac{u_i}{U_0}, & \sigma_i^* &= \frac{\sigma_i}{\rho U_0^2}, & p^* &= \frac{p}{\rho U_0^2}, & t^* &= \frac{t U_0}{D}, \\ l^* &= \frac{l}{D}, & x^* &= \frac{x}{D}, & y^* &= \frac{y}{D}, & (i = 1, 2), \end{aligned} \quad (3)$$

where the non-dimensional parameters, such as the initial tension T , the curvature κ , the density of the beam ρ_m , the wall stiffness EA , EJ , and the Reynolds number are similarly scaled as

$$\begin{aligned} T^* &= \frac{T}{\rho U_0^2 D}, & \kappa^* &= \kappa D, & \rho_m^* &= \frac{\rho_m}{\rho D}, & c_\lambda &= \frac{EA}{\rho U_0^2 D}, \\ c_\kappa &= \frac{EJ}{\rho U_0^2 D^3}, & Re &= \frac{U_0 D \rho}{\mu}. \end{aligned} \quad (4)$$

The variables with a star are the non-dimensional ones, which will be used throughout this paper. In the following, however, the stars are dropped for simplicity.

Note c_λ and c_κ are not independent to each other, and they are related by

$$c_\kappa = c_\lambda \frac{A^2}{12D^2}. \quad (5)$$

We define the principal stretch $\lambda = \sqrt{x'^2 + y'^2}$ and wall curvature $\kappa = \frac{x'y'' - y'x''}{\lambda^3}$, where $x = x(l, t)$, $y = y(l, t)$, l is the x coordinate in the undeformed configuration, and the prime denotes differentiation with respect to l . Using the Kirchhoff constitutive laws for the elastic beam, and dropping the stars for convenience, we write the dimensionless governing equations for the beam (for derivation of these, see [24]):

$$\frac{\rho_m}{\lambda} \left(x' \frac{d^2x}{dt^2} + y' \frac{d^2y}{dt^2} \right) = c_\kappa \kappa \kappa' + c_\lambda \lambda' + \lambda \tau_n = 0, \quad (6)$$

$$\frac{\rho_m}{\lambda} \left(y' \frac{d^2x}{dt^2} - x' \frac{d^2y}{dt^2} \right) = c_\kappa \left(\frac{1}{\lambda} \kappa' \right)' - \lambda \kappa T - c_\lambda \lambda \kappa (\lambda - 1) - \lambda \sigma_n + \lambda p_e = 0, \quad (7)$$

$$194 \quad x' = \lambda \cos \theta, \quad y' = \lambda \sin \theta, \quad \theta' = \lambda \kappa. \quad (8)$$

195 And the fluid flow obeys the Navier–Stokes equations:

$$196 \quad \frac{\partial u_i}{\partial t} + u_j u_{i,j} = -p_{,i} + \frac{1}{Re} u_{i,jj}, \quad (9)$$

$$198 \quad u_{i,i} = 0, \quad i, j = 1, 2 \quad (10)$$

199 where θ is the rotating angle of the beam in the horizontal
200 position, σ_n and τ_n are the normal and shear stresses of
201 fluid on the beam which can be expressed as

$$203 \quad \sigma_n = p - \frac{2}{Re} \frac{\partial u_n}{\partial n}, \quad \tau_n = -\frac{1}{Re} \left(\frac{\partial u_s}{\partial n} + \frac{\partial u_n}{\partial s} \right) \quad (11)$$

204 where s and n indicate the tangential and the normal direc-
205 tion of the beam. Note that as both c_κ and $c_\lambda \rightarrow 0$, we re-
206 cover the fluid-membrane model [8].

207 Boundary conditions for the flow field are chosen such
208 that steady parabolic velocity profile is used for the
209 upstream inlet, the stress free condition for the downstream
210 outlet, and the no-slip condition is used along the walls
211 including the elastic section. Clamped conditions are used
212 for the two ends of the beam.

213 It is important to note that on deriving (6) and (7), the
214 initial stress configuration is used, i.e., all deformations
215 are defined with the length L in Fig. 3, thus $\lambda = \lambda_x$, and
216 the initial stress is $\sigma_0 = T/A$.

217 3.2. The Adina models

218 To compare our results with Adina (version 8.2), we
219 rebuild the fluid-beam configuration (Fig. 2) using Adina's
220 fluid structure interaction solver [28]. The governing equa-
221 tions for the fluid are the same as Eqs. (9) and (10). For the
222 structure, we solve a plane strain problem (as in the fluid-
223 beam formulation); only a slice of structure with unit thick-
224 ness is considered, and all strains components in z -direction
225 are zero. Thus the governing equation is derived from the
226 principle of virtual work:

$$229 \quad \int_V \tau_{ij} \delta e_{ij} dV = \int_S f^s \delta u^s dS \quad i, j = 1, 2 \quad (12)$$

230 where τ_{ij} is the Cauchy stress tensor, e_{ij} is the strain tensor
231 corresponding to virtual displacements, and V is the vol-
232 ume, S is the surface on which external traction (pressure)
233 f^s is applied, and δu^s are the components of virtual dis-
234 placement vector evaluated on the surface S . When there
235 is an initial tension, this can be specified with the initial
236 strain approach, i.e., an initial strain, e_{11} , in the x -direction
237 is added to the strain tensor e_{ij} , which is defined with the
238 initial resting length of the beam, l_0 . Alternatively, this
239 can be specified with the initial stress approach, i.e., the ini-

tial stress $\sigma_{11} = \frac{T}{A}$ is added to the stress tensor σ_{ij} , and e_{ij} is
240 now defined with the length l [30]. 241

For the two-dimensional beam, (12) is evaluated with a
242 unit length in z -direction, and can be written as [30] 243

$$244 \quad EJ \int \frac{d\beta}{dx} \frac{d\delta\beta}{dx} dx + GSk \int \left(\frac{dw}{dx} - \beta \right) \left(\frac{d\delta w}{dx} - \delta\beta \right) dx \\ = \int f \delta w dx + \int m \delta\beta dx \quad (13) \quad 246$$

247 where f and m are the transverse and moment loadings per
248 unit length, EJ is the wall stiffness, w and β are the displace-
249 ment and total rotation of the mid-plane which is assumed
250 to remain a plane after deformation. G is the shear modu-
251 lus, S is the cross-sectional area, and k is a shear constant
252 which is $5/6$ for a rectangular cross-section [30]. Note the
253 second term in (13) represents the shear effect [30], which
254 is considered to be small for a thin beam and is ignored
255 in our formulation [24]. Note if the initial stress approach
256 is used, the final equations Adina solves is almost identical
257 (except the shear effect) to the fluid-beam model, thus the
258 results from these two models should be the more or less
259 the same. However, if the initial strain configuration is
260 used, then these two formulations are different unless the
261 initial strain is zero (i.e. $\lambda_0 = 1$). Results from both initial
262 configurations will be computed and compared with those
263 from the fluid-beam model.

264 4. Numerical methods

265 4.1. Numerical methods for the fluid-beam model

266 A finite element code for unsteady flow is developed to
267 solve the coupled non-linear fluid–structure interactive
268 equations simultaneously, and an adaptive mesh with
269 rotating spines is used to allow for a movable boundary.
270 The mesh is divided into three subdomains, one of which
271 is placed with many spines originating from the bottom
272 rigid wall to the movable beam [24]. These spines are
273 straight lines, which can rotate around the fixed nodes at
274 the bottom. Thus all the nodes on the spines can be
275 stretched or compressed depending on the beam deforma-
276 tion. A numerical code is developed to solve the fluid and
277 the beam equations simultaneously using weighted residual
278 methods.

279 A Petrov–Galerkin method is used to discretise the sys-
280 tem Eqs. (6)–(10). The element type for flow is 6-node tri-
281 angular with second order shape function N_i for u and v ,
282 and linear shape function L_i for p . Three-node beam ele-
283 ments with second order shape function are used for x , y ,
284 θ , λ and κ . The discretised finite element equations can
285 be written in a matrix form as

$$287 \quad M(U) \frac{dU}{dt} + K(U)U - F = R = 0 \quad (14)$$

288 where $U = (u_j, v_j, p_j, x_j, y_j, \theta_j, \lambda_j, \kappa_j)$ is the global vector of
289 unknowns, and $j = 1, \dots, n$, is the nodal number. \mathbf{R} is the
290 overall residual vector denoted by

$$292 \quad R = (R_x, R_y, R_c, R_{e_x}, R_{e_y}, R_{e_\lambda}, R_{e_\kappa}), \quad (15)$$

293 where the subscripts x , y , c indicate the corresponding
294 residuals of the x and y -momentum and continuity in fluid,
295 and $e_x, e_y, e_\theta, e_\lambda, e_\kappa$ indicate the corresponding residuals of
296 Eqs. (6)–(10).

297 An implicit finite difference second order predictor-corrector
298 scheme with a variable time step is used to solve the
299 time dependent problem. At each time step, the frontal
300 method and a Newton–Raphson scheme are employed to
301 obtain the converged solution for the whole system
302 simultaneously.

303 4.2. Numerical accuracy for the fluid-beam model

304 Validations for the fluid-beam model have been per-
305 formed extensively where a grid size ratio was given based
306 on the boundary thickness [24]. In this study, two different
307 grids are used. Grid B, the coarser one, where only
308 $16 \times (20 + 60 + 60)$ elements are used with the stretch ratio
309 of 1:10 towards the corners, is initially used for all simula-
310 tions. Grid A, a more refined one, which can solve for the
311 smallest value of the extensional stiffness parameter is used
312 to rerun the steady and unsteady simulations when large
313 deformation occurs. In this case, the smallest boundary
314 layer width is estimated to be about 0.0141, and the grid
315 is chosen to be $22 \times (70 + 120 + 200)$ with the same stretch
316 ratio towards the two corners where the beam joins the
317 rigid wall in both directions. The computations are per-
318 formed on Euclid2, a twin PentiumIV processors
319 (3.4 GHz) Linux machine with 8GB memory at Glasgow
320 University, and take about 0.1–1 CPU min for a typical
321 steady solution.

322 4.3. Numerical methods for Adina model

323 Here we solve a large deformation, small strain problem
324 by using a total lagrange formulation [30]. For the elastic
325 wall, 3-node isoparametric beam elements are used, which
326 allows for large displacement with small strains, and 3-
327 node triangle elements are used for the fluid (as Adina
328 8.3 do not have 6-node triangle fluid element). A typical
329 mesh used is shown in Fig. 4.

330 A movable mesh was used over the fluid domain, so as
331 to increase the accuracy of the calculations as the flexible
332 wall moved.

333 The finite element equations for the coupled fluid–struc-
334 ture system are derived from the Pertov–Galerkin varia-
335 tional formulation, which are solved using either an
336 iterative or a direct approach [29]. For the iterative

method, the fluid and structural domains are treated sepa- 337
rately, using the most recent solution for one domain to 338
obtain the solution for the other domain. These iterations 339
are carried out until the coupled equations were satisfied. 340
For the direct method, the fluid and structural equations 341
are combined into a matrix system of equations and solved 342
simultaneously. The direct method requires more memory, 343
but is faster than the iterative method. However, in cases 344
where the beam deformation was large, the direct method 345
fails to give convergence and the iterative approach has 346
to be used. Solutions of the matrix equations are obtained 347
using a sparse matrix direct solver based on Gaussian elim- 348
ination [28]. 349

Results for steady simulations are obtained starting with 350
an initially undeformed channel, with the flexible beam 351
aligned with the upper channel wall. Because of difficulties 352
in obtaining converged solutions, due to the non-linearities 353
associated with large beam deformations, it was necessary 354
to apply the inlet flow and the external pressure incremen- 355
tally. This minimized any element distortion normally asso- 356
ciated with rapid mesh deformation. 357

4.4. Numerical accuracy for Adina model 358

In order to verify the grid independence, meshes with 359
different numbers of elements were used and the results 360
compared. These verification studies were carried out with 361
zero pre-tension in the beam and for the Young’s modulus 362
of 35.89 kPa, and $c_\lambda = 500$. Each mesh was checked by 363
increasing the grid points of previously tested mesh. This 364
was continued until the changes of both the maximum dis- 365
placement of the beam and the maximum pressure in the 366
flow domain are within 0.5% between different meshes. 367
These results were also verified by comparing them to the 368
results obtained by Luo and Pedley [8]. The mesh eventu- 369
ally used had 26,839 elements. 370

371 5. Results

372 5.1. Parameters

Following [24], the dimensionless parameters are chosen 373
to be 374

$$375 \quad Re = 300, \quad D = 1, \quad L_u = 5, \quad L = 5, \quad L_d = 30, \quad p_e = 1.95, \\ 376 \quad \rho_m = 0, \quad c_\lambda = 1 - 1000, \quad A/D = 0.01 - 0.1, \quad T_0 = 178.8,$$

where $\beta (>0)$ was used by Luo and Pedley [17] to scale 377
tension: $T = T_0/\beta$. When $\beta \rightarrow \infty$, $T = 0$. A/D is the ratio 378
between the beam wall thickness and the channel height. 379



Fig. 4. A typical mesh for the deformed system in the Adina model.

380 These need to be converted to dimensional parameters used
 381 by Adina. The required input parameters for Adina are the
 382 inlet velocity U_0 , the external pressure P_e , the initial strain
 383 ε , the Young's modulus E , the channel depth, and the wall
 384 thickness A . These can be obtained from our dimensionless
 385 parameters as follows:

$$U_0 = \frac{Re \times \mu}{\rho \times D}, \quad P_e = p_e \rho U_0^2, \quad E = \frac{c_\lambda \rho U_0^2 D (1 - \nu^2)}{A},$$

$$T = (T_0/\beta) \times \rho U_0^2 D, \quad \varepsilon = \frac{T}{EA} \quad (16)$$

389 where the Poisson's ratio ν is chosen to be 0.45, density of
 390 fluid ρ is 1000 kg/m³, the viscosity of fluid μ is 0.001 Pa·s,
 391 the channel height D is 0.01 m, and the channel depth (in
 392 z -direction) is 1 m. For example, when $Re = 300$, $p_e =$
 393 1.95, $c_\lambda = 1000$, $\beta = 90$, and $A/D = 0.01$, (16) gives

$$U_0 = 0.03 \text{ m}, \quad P_e = 1.755 \text{ Pa}, \quad E = 71.775 \text{ kPa},$$

$$A = 0.0001 \text{ m}, \quad \varepsilon = 0.0024911.$$

396 5.2. Effects of initial strain and initial stress configurations

397 First, consider a thin wall and choose $c_\kappa = 10^{-5} c_\lambda$, i.e., A
 398 is about 1% of the channel height. The computed elastic
 399 wall shapes for $c_\lambda = 200, 500$ and 1000, and different values
 400 of the initial tension (indicated by the values of β) are
 401 shown in Figs. Figs. 5a–c.

402 For $T=0$ ($\beta = \infty$), all three approaches (fluid-beam
 403 model, Adina initial stress, Adina initial strain) give the
 404 same results for $c_\lambda = 500$, and $c_\lambda = 1000$. However, some
 405 differences are observed when $c_\lambda = 200$ between our results
 406 and that of Adina. This is presumably because Adina con-
 407 sidered the shear effect, which is absent in our model. When
 408 the stretching stiffness is smaller, the shear effect becomes
 409 more significant. Therefore the deformation predicted by

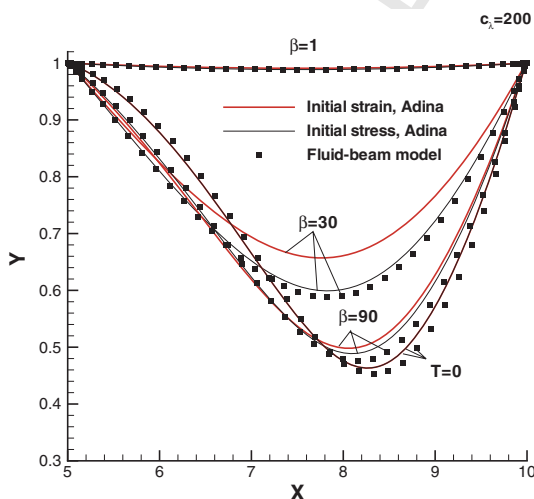


Fig. 5a. The elastic wall shapes for $c_\lambda = 200$, and $\beta = 1, 30, 60, 90, \infty$ ($T=0$). The thicker solid lines are results from Adina with initial strain, and the thinner solid lines are from Adina with initial stress. The symbols are from the fluid-beam model.

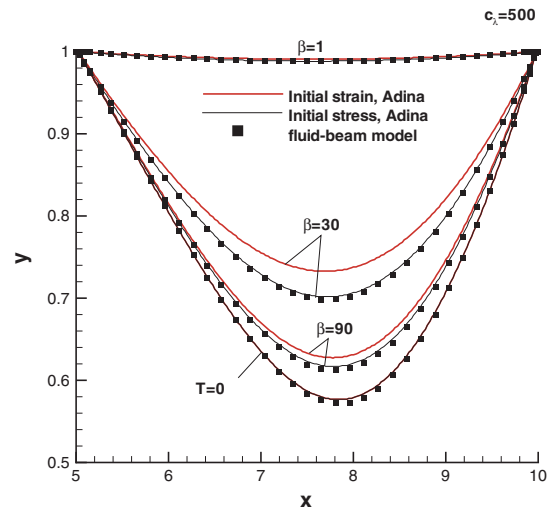


Fig. 5b. The elastic wall shapes for $c_\lambda = 500$, and $\beta = 1, 30, 60, 90, \infty$ ($T=0$). The thicker solid lines are results from Adina with initial strain, and the thinner solid lines are from Adina with initial stress. The symbols are from the fluid-beam model.

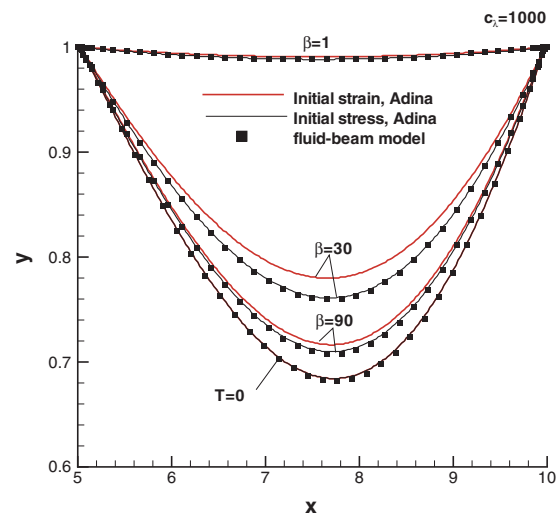


Fig. 5c. The elastic wall shapes for $c_\lambda = 1000$, and $\beta = 1, 30, 60, 90, \infty$ ($T=0$). The thicker solid lines are results from Adina with initial strain, and the thinner solid lines are from Adina with initial stress. The symbols are from the fluid-beam model.

Adina is slightly smaller. However, in general, our fluid-beam model agrees very well with Adina when the initial stress configuration is used.

Now we can compare the results using the initial stress (Adina and fluid-beam) and initial strain (Adina) configurations. When $T=0$, these two configurations give identical results for all values of c_λ studied (at least for Adina). Interestingly, the results between the initial stress and initial strain approaches start to differ as the initial tension is increased, in both cases $\beta = 30$, and 90, the initial strain approach gives less deformation compared with that of the initial stress configuration. However, for $\beta = 1$ (i.e. the tension is very high), as the total deformation is now small, the differences between these two configurations become less

424 significant again. Thus for small deformation, the choice of
425 the initial configurations is less important. This justifies the
426 results from many previous studies using the initial stress
427 approach. However, for large deformation, the difference
428 between these two configurations is noticeable.

429 The corresponding streamlines and pressure contours
430 predicted by both Adina (with the initial strain configura-
431 tion) and the fluid-beam model are shown in Figs. 6 and 7
432 for $c_\lambda = 500$, and $c_\lambda = 1000$, respectively. It can be seen that
433 the results are again similar (though the scaling is not
434 exactly the same as these plots are output from two differ-
435 ent software). The strength and range of the flow re-circula-
436 tion is predicted by both models (though the fluid-beam
437 model has less smooth stream functions due to the simple

interpolations used). As the fluid-beam model gives slightly
438 greater wall deformation (see Figs. 5b and c), this is
439 reflected in the pressure field especially underneath the max-
440 imum deformation of the wall. The shaded semi-circle area
441 (indicating the lowest pressure zone) is also larger in the
442 fluid-beam model than in the Adina model. This is more
443 obvious for $c_\lambda = 500$, as the differences in initial stress and
444 initial strain configurations must be greater for lower values
445 of c_λ .
446

5.3. The wall thickness effect 447

As all our previous results are obtained for a very thin
448 wall thickness ($A \approx 1\%$), it is constructive to provide a set
449

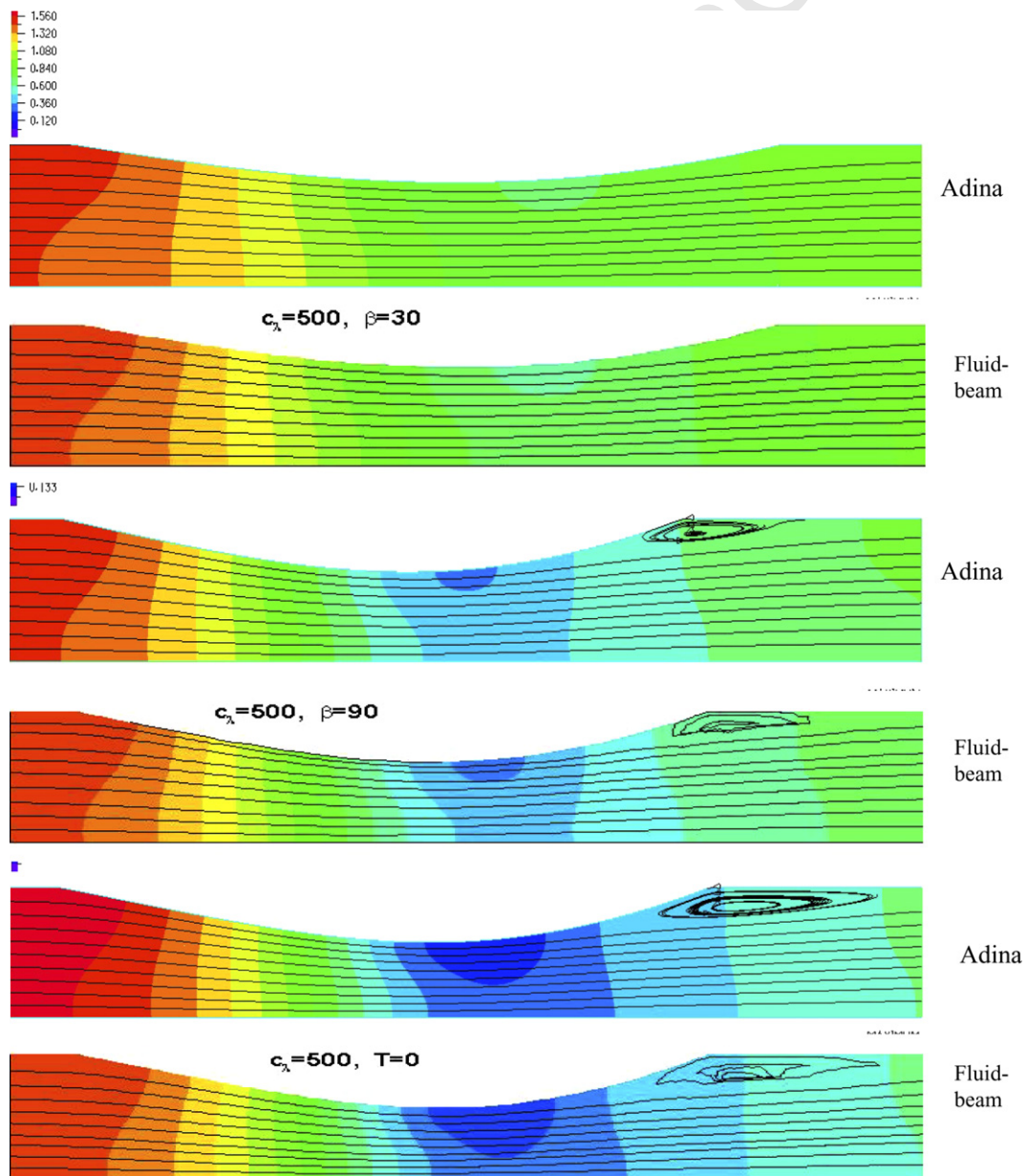


Fig. 6. Streamlines for $c_\lambda = 500$, and $\beta = 30, 60, 90$, and $T = 0$. Overlapped are the corresponding pressure contours with bright colour indicating the higher pressure contour values.

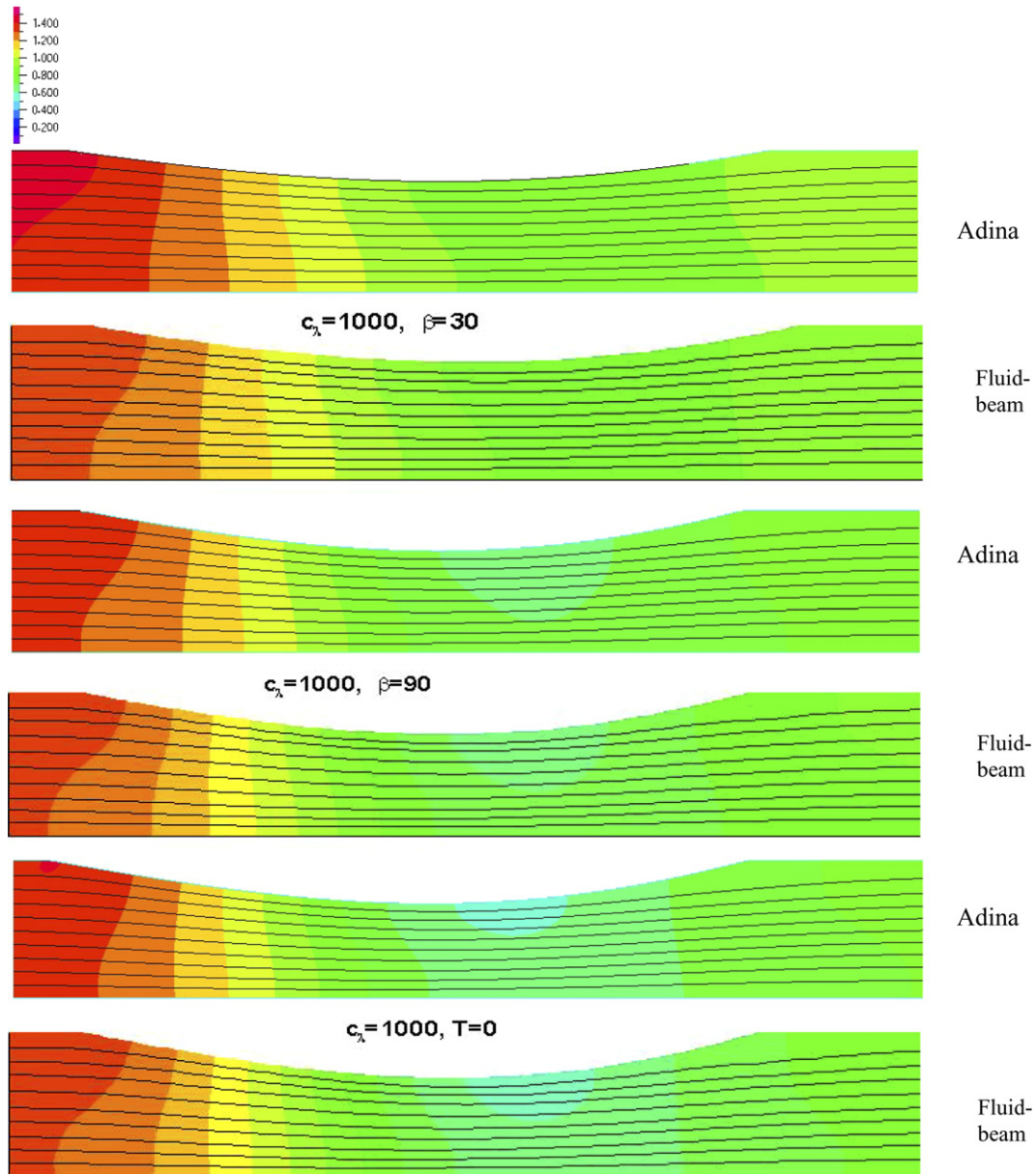


Fig. 7. Streamlines for $c_\lambda = 1000$, and $\beta = 30, 90$, and $T = 0$. Overlapped are the corresponding pressure contours with bright colour indicating the higher pressure contour values.

450 of solutions for different values of wall thickness. In doing
451 so, we keep the Young's modulus E fixed ($=35.9$ kPa), and
452 vary the wall thickness A from 1%, to 2%, 4%, 6%, 8% and
453 10% of the channel height, respectively. This implies that in
454 the fluid-beam model, both c_λ and c_κ are changed accord-
455 ingly, see Eq. (16), (e.g. $c_\lambda \approx 500$ for $A = 1\%$). The elastic
456 wall shapes thus obtained are shown in Fig. 8. The solid
457 curves are from Adina with the initial strain configura-
458 tion, and the symbols are from the fluid-beam model.
459 Again, the agreement between the two models for $T = 0$
460 is excellent.

461 The same results are shown in Fig. 9 but with an initial
462 tension, $\beta = 30$. The differences between these two models
463 (Adina uses the initial strain configuration and fluid-beam

is the initial stress configuration) become less and less 464
noticeable as the wall thickness is increased from 1% to 465
10%. This is because the corresponding values of c_λ are 466
greater in the thicker walled beam, and the initial tension 467
chosen becomes less dominant compared with the stretch 468
induced tension. 469

6. Discussion 470

We have successfully re-produced all our results using 471
Adina with initial stress formulation. Initial stress 472
approach is commonly used in many engineering applica- 473
tions where the previous loading history is unknown. How- 474
ever, the initial strain approach is defined more rigorously 475

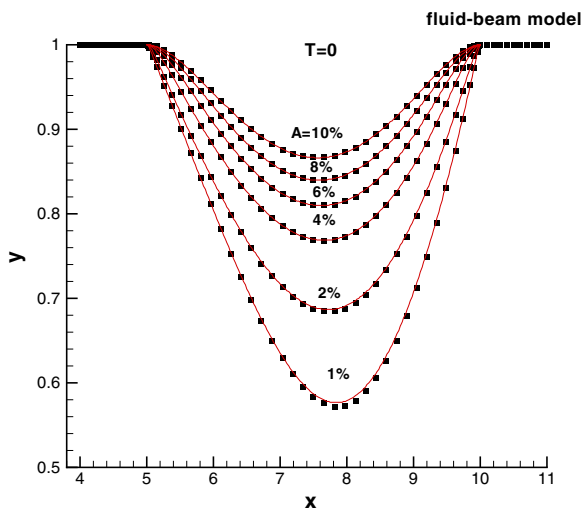


Fig. 8. Elastic wall shapes for different wall thickness obtained from the fluid-beam (symbols) and Adina initial strain (solid line), all with Young's modulus $E = 35.9$ kPa, and $T = 0$.

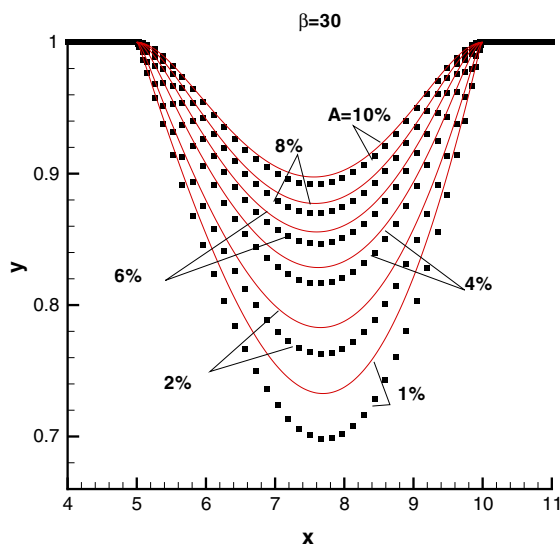


Fig. 9. As in Fig. 8, but with $\beta = 30$.

476 in the sense that all equations are derived from the zero initial
477 initial stress configurations. Thus when the eigenvalue problem
478 is solved [1], it may be essential that the initial strain
479 configuration is used.

480 The key finding is that although the differences from
481 these two initial configurations are small for the collapsible
482 channel with small deformation, there are sufficient
483 changes in the steady solutions using these two configura-
484 tions when the deformation is larger. These could lead to
485 different results in the stability analysis, as the basic flow
486 is slightly changed.

487 To make sure that the initial configuration is not respon-
488 sible for the "tongue" observed in the neutral stability
489 curve, we re-solve the eigenvalue problem with a zero initial
490 tension, and then see if the "tongue" still occur. Note that

491 in order to compare the new results with Fig. 1, we need to
492 use the concept of the effective tension, which is defined as
493 [24]:

$$T_{\text{eff}} = T_0 + c_\lambda(\lambda - 1), \quad (17)$$

494 where λ is the principal stretch ($=\lambda_x$) defined in Section 3.1.
495 Since the principal stretch λ varies along the beam, we need
496 to estimate the effective tension by calculating λ at a fixed
497 station along the beam, say at the downstream end (calculating
498 λ at any other position does not change the results
499 significantly).
500

501 We would like to emphasize that the introduction of the
502 effective tension is essential here since our new results are
503 obtained for a zero initial tension. As defined in Eq. (17),
504 the effective tension is the measure of the real tension that
505 the beam experiences, whether or not the initial tension is
506 zero. In the earlier study where the "tongue" was found,
507 the initial tension was not zero. The use of the effective ten-
508 sion makes the two cases comparable. In other words, we
509 need to plot both the neutral stability curves in the $Re-T_{\text{eff}}$
510 space. Thus in scenario A, we prescribe T_0 and replot the
511 neutral curve from Fig. 1 in the $Re-T_{\text{eff}}$ space, and in scenar-
512 io B, we let $T_0 = 0$, but adjust c_λ so that a same value of
513 T_{eff} can be calculated from (17). All other parameters
514 are kept the same. The results thus computed are shown
515 in Fig. 10. For details of the eigenvalue problem, see [1,31].
516

517 It is highly interesting to see that although the new neutral
518 curve (solid) is shifted downwards slightly in the
519 $Re-T_{\text{eff}}$ space (partly due to the small differences in basic
520 flows using different initial configurations, and partly due
521

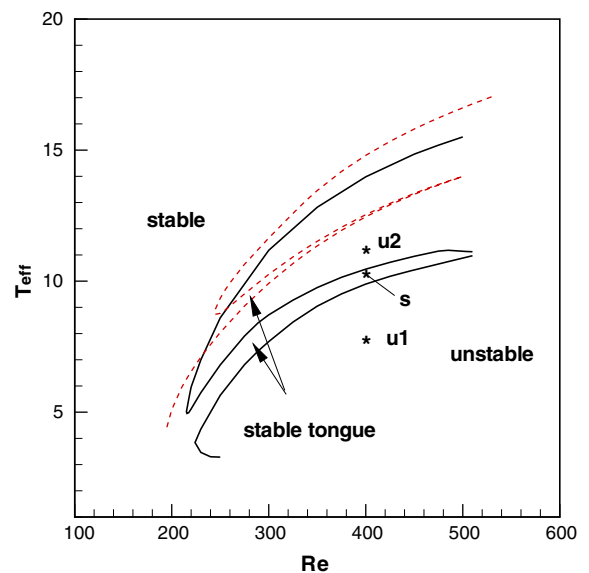


Fig. 10. The neutral stability curves in the $Re-T_{\text{eff}}$ space. The solid curve is the new results obtained with a zero initial tension, while the dashed one is the one corresponding to Fig. 1. The three points $u1$, s , and $u2$ have the corresponding coordinates of $Re = 400$, and $T_{\text{eff}} = 7.67, 10.19$, and 8.45 ($c_\lambda = 310, 380$ and 500), respectively.

522 to the fact that a finer mesh is used for the new results here
 523 for the eigensolver), the two curves are very similar, both
 524 present the same qualitative features, i.e., both have the
 525 “tongue” structure. The first implication of this is that
 526 the concept of the effective tension is robust, and can be
 527 used as a key control parameter for the system. The other,
 528 more important implication, is that the “tongue” still
 529 exists, showing that it is not due to the fact the initial stress
 530 configuration was used.

531 It may be said that a better way to check the tongue’s
 532 existence is to simply run the unsteady simulations, and
 533 see if the solutions around this zone present same behav-
 534 iour as predicted by Fig. 10. However, care should be taken
 535 here as the unsteady simulations are also obtained from the
 536 governing equations based on the initial stress configura-
 537 tions (unless T is zero), thus may suffer the same problem.

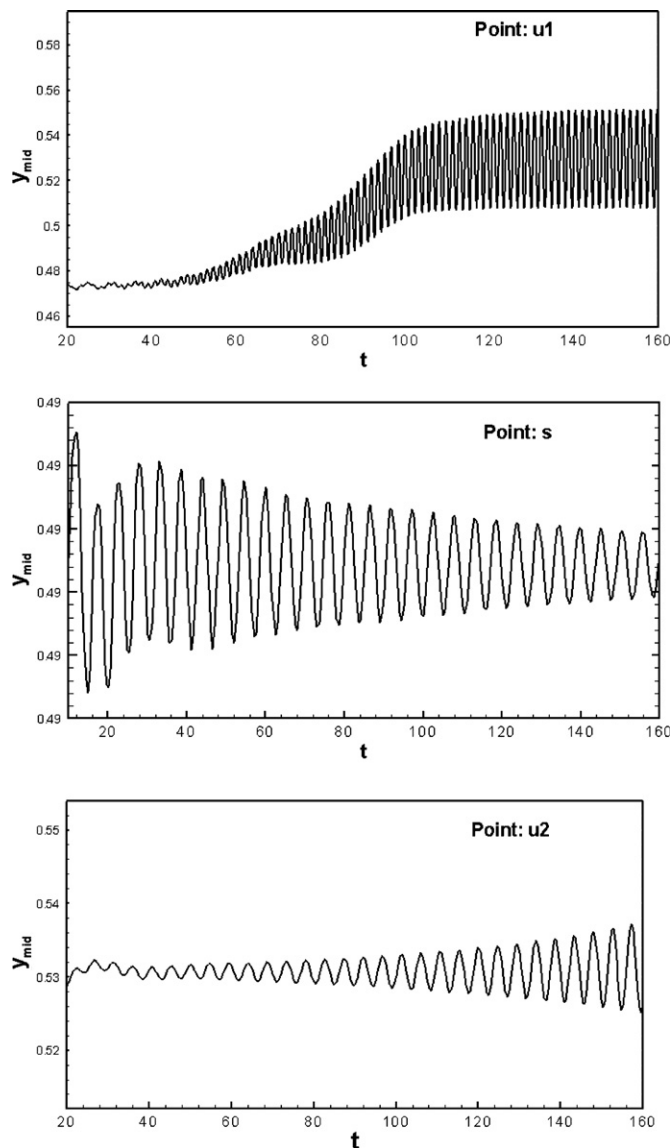


Fig. 11. The unsteady solutions at the three points $u1$, s , and $u2$ across the tongue zone, as shown in Fig. 10. Plotted is the y -displacement initially at the middle point of the beam against time.

Now that we have obtained the new neutral curve, we can
 run the unsteady simulations with the zero initial tension.
 Take the points $u1$, s , and $u2$ in Fig. 10, for example. If
 the tongue is true, then the unsteady solutions at $u1$, and
 $u2$ should be unstable, while at point s it should be stable.
 To obtain these solutions, an initial perturbation is applied
 to the corresponding steady solutions at these points, and
 the time response of the system is obtained. The results
 are shown in Fig. 11. The wall displacement in the y -direc-
 tion at the mid-point of the beam initially is plotted against
 time. It is seen that the solution at s is indeed stable, as the
 perturbation decays with time. The solution at $u2$ it is
 indeed unstable, and the self-excited oscillation is devel-
 oped and is growing with time. However, from the
 unsteady simulation it is harder to see that if solution at
 $u1$ is unstable or not in the longer term, since its growth
 rate seems to be very small. This is presumably because it
 is closer to the neutral curve than $u2$. It is for this reason,
 we could not use the unsteady simulations alone to deter-
 mine the neutral curve, as on the neutral curve, all solu-
 tions have a zero growth rate, and an infinitely long time
 would be required to determine the growth rate. However,
 it is encouraging that the unsteady simulations support the
 existence of the tongue.

7. Conclusion

The effects of the initial configurations on the steady
 solutions and the neutral stability curve of flow in collaps-
 ible channel are studied in this paper. Two independent
 numerical models are employed. One is the fluid-beam
 model [24]; the other is the iso-beam model (with a fluid-
 structure interaction solver) from the Adina with both
 the initial strain and initial stress configurations. As
 expected, the fluid-beam model agrees very well with Adina
 for the initial stress configuration; however, they differ
 when the initial strain configuration is used. The differences
 in the steady solutions between these two configurations
 are small if either the deformation is very small (tension
 is large) or the initial tension is small compared with the
 stretched induced tension. However, when these conditions
 are not met, there are some discrepancies between these
 two, suggesting that the principal stretch needs to be
 defined properly with the (zero-stressed) initial length.
 The most important finding is that we found that the same
 stability “tongue” exists in the Reynolds number-effective
 tension space, regardless of the initial configuration used.
 This is also supported by the full unsteady numerical sim-
 ulations. Thus although a complete physical explanation of
 the “tongue” remains to be found, this work suggests
 that the “tongue” presents a real and interesting physical
 phenomenon.

8. Uncited references

[3,4,5,6,7,9,10,11,12,21,22,23,26,27].

590 **Acknowledgements**

591 This work is supported by the EPSRC (Grant No. GR/
592 M07243) and the Royal Society of London (2005/R4-JP).
593 Special thanks to Prof. R. Ogden and Prof. ZX Cai for use-
594 ful discussions.

595 **References**

- 596 [1] Luo XY, Cai ZX. Effects of wall stiffness on the linear stability of
597 flow in an elastic channel. In: de Langre E, Axisa F, editors.
598 Proceedings of the eighth international conference on fluid induced
599 vibrations, FIV2004, vol. II. Paris, France: 2004, p. 167–70.
600 [2] Shapiro AH. Steady flow in collapsible tubes. ASME J Biomech Eng
601 1977;99:126–47.
602 [3] Grotberg JB, Gavriely N. Flutter in collapsible tubes: a theoretical
603 model of wheezes. J Appl Physiol 1989;66:2262–73.
604 [4] Kamm RD, Pedley TJ. Flow in collapsible tubes: a brief review.
605 ASME J Biomech Eng 1989;111:117–79.
606 [5] Jensen OE, Pedley TJ. The existence of steady flow in a collapsed
607 tube. J Fluid Mech 1989;206:339–74. 623–59.
608 [6] Matsuzaki Y, Fujimura K. Reexamination of steady solutions of a
609 collapsible channel conveying fluid, a technical brief. ASME J
610 Biomech Eng 1995;117:492–4.
611 [7] Grotberg JB. Pulmonary flow and transport phenomena. Annu Rev
612 Fluid Mech 1994;26:529–71.
613 [8] Luo XY, Pedley TJ. A numerical simulation of steady flow in a 2D
614 collapsible channel. J Fluids Struct 1995;9:149–74.
615 [9] Pedley TJ, Luo XY. Modelling flow and oscillations in collapsible
616 tubes. Theor Comp Fluid Dyn 1998;10:277–94.
617 [10] Davies C, Carpenter PW. Instabilities in a plane channel flow
618 between compliant walls. J Fluid Mech 1997;352:205–43.
619 [11] Davies C, Carpenter PW. Numerical simulation of the evolution of
620 Tollmien–Schlichting waves over finite compliant panels. J Fluid
621 Mech 1997;335:361–92.
622 [12] Heil M. Stokes flow in collapsible tubes: computation and experi-
623 ment. J Fluid Mech 1997;353:285–312.
624 [13] Bertram CD. Two modes of instability in a thick-walled collapsible
625 tube conveying a flow. J Biomech 1982;15:223–4.
- [14] Bertram C, Raymond, Pedley TJ. Mapping of instabilities for flow
626 through collapsed tubes of differing length. J Fluid Struct
627 1990;4:125–53.
628 [15] Jensen OE. Instabilities of flow in a collapsed tube. J Fluid Mech
629 1990;220:623–59.
630 [16] Jensen OE. Chaotic oscillations in a simple collapsible tube model.
631 ASME J Biomech Eng 1992;114:55–9.
632 [17] Luo XY, Pedley TJ. A numerical simulation of unsteady flow in a 2D
633 collapsible channel. J Fluid Mech 1996;314:191–225.
634 [18] Luo XY, Pedley TJ. The effects of wall inertia on flow in a 2-D
635 collapsible channel. J Fluid Mech 1998;363:253–80.
636 [19] Luo XY, Pedley TJ. Flow limitation and multiple solutions in 2-D
637 collapsible channel flow. J Fluid Mech 2000;420:301–24.
638 [20] Jensen OE, Heil MH. High frequency self-excited oscillations in a
639 collapsible-channel flow. J Fluid Mech 2003;481:235–68.
640 [21] Hazel AL, Heil MH. Steady finite-Reynolds-number flows in three-
641 dimensional collapsible tubes. J Fluid Mech 2003;486:79–103.
642 [22] Marzo A, Luo XY, Bertram CD. Three-dimensional flow through a
643 thick-walled collapsible tube. J Fluid Struct 2005;20:817–35.
644 [23] Heil M, Waters SL. Transverse flows in a rapidly oscillating, elastic
645 cylindrical shells. J Fluid Mech 2006;547:185–214.
646 [24] Cai ZX, Luo XY. A fluid-beam model for flow in a collapsible
647 channel. J Fluid Struct 2003;17:125–46.
648 [25] Steigmann DJ, Ogden RW. Plane deformations of elastic solids with
649 intrinsic boundary elasticity. Proc R Soc London A 1997;453:853–77.
650 [26] Carpenter PW, Garrard AD. The hydrodynamic stability of flow over
651 Kramer-type compliant surfaces. Part 2. Flow-induced surface
652 instabilities. J Fluid Mech 1986;170:188–232.
653 [27] Ehrenstein U, Koch W. Three dimensional wavelike equilibrium
654 states in plane Poiseuille's flow. J Fluid Mech 1989;228:111–48.
655 [28] ADINA theory and modelling guide, vol. 1–3. ADINA R&D Inc.;
656 2003.
657 [29] Bathe KJ, Zhang H. Finite element development for general fluid
658 flows with structural interactions. Int J Numer Meth Eng
659 2004;60:213–32.
660 [30] Bathe KJ. The finite element procedures. Englewood Cliffs, NJ: Pren-
661 tice-Hall Inc.; 1996.
662 [31] Luo XY, Cai ZX, Li WG, Pedley TJ. On the cascade structure of
663 stability of flow in collapsible channels. J Fluid Mech [submitted for
664 publication].
665
666